Measuring Stratospheric H_2O with an Airborne Spectrometer

MAZIAR BANI SHAHABADI AND YI HUANG

Department of Atmospheric and Oceanic Science, McGill University, Montreal, Quebec, Canada

(Manuscript received 30 August 2013, in final form 1 April 2014)

ABSTRACT

This study examines the ability of an infrared spectral sensor flying at the tropopause level for retrieving stratospheric H_2O. Synthetic downwelling radiance spectra simulated by the line-by-line radiative transfer model are used for this examination. The potential of high-sensitivity water vapor retrieval is demonstrated by an ideal sensor with low detector noise, high spectral resolution, and full infrared coverage. A suite of hypothetical sensors with varying specifications is then examined to determine the technological requirements for a satisfactory retrieval. This study finds that including far infrared in the sensor's spectral coverage is essential for achieving accurate H_2O retrieval with an accuracy of 0.4 ppmv (1-sigma). The uncertainties in other gas species such as CH_4, N_2O, O_3, and CO_2 do not significantly affect the H_2O retrieval. Such a hyperspectral instrument may afford an advantageous tool, especially for detecting small-scale lower-stratospheric moistening events.

1. Introduction

Stratospheric water vapor (H_2O) radiatively cools the stratosphere but warms the troposphere. Previous studies have shown that stratospheric H_2O is a contributor to Earth climate change. Forster and Shine (1999) show that, although the observed cooling of the lower stratosphere is thought to be due to the combination of stratospheric ozone (O_3) loss and carbon dioxide (CO_2) increase, the increase in stratospheric H_2O may be capable of producing as much of the observed cooling as the O_3 loss does. Solomon et al. (2010) show that stratospheric H_2O may even be an important driver for surface climate change. They argue that a 10% decrease of stratospheric H_2O after the year 2000 acted to slow the rate of global surface warming from 2000–09 by 25% compared to what would have occurred due to only greenhouse gases. Moreover, Anderson et al. (2012) suggest that there is an increased risk of O_3 loss from lower-stratospheric moistening.

Various approaches have been adopted for measuring the stratospheric H_2O. Before the 1990s the information was largely based on localized balloonborne measurements (e.g., Oltmans et al. 2000). It has been a concern as to how well the changes in stratospheric H_2O can be monitored due to calibration issues and limited spatial coverage (Kley et al. 2000). Although a variety of techniques—for example, the Harvard Lyman-alpha and Jet Propulsion Laboratory laser hygrometers—have been developed, the intercalibration between the instruments remains an issue (e.g., Weinstock et al. 2009). After the 1990s high-quality satellite observations, including the Stratospheric Aerosol and Gas Experiment II (SAGE II) (Thomason et al. 2004), the Halogen Occultation Experiment (HALOE) (Russell et al. 1993), the Microwave Limb Sounder (MLS)/Upper Atmosphere Research Satellite (UARS) (Livesey et al. 2003), and Atmospheric Chemistry Experiment–Fourier transform spectrometer (ACE-FTS) (Bernath et al. 2005), began to collect information about stratospheric H_2O. Satellites have the capacity to cover the globe and measure multiple species simultaneously, which renders them efficient monitoring tools. However, limb and occultation sounders that are sensitive to stratospheric water vapor have large sampling footprints, which makes small-scale water vapor variation, for example, induced by convective moistening, hardly detectable (Schwartz et al. 2013). Moreover, satellite remote sensing relies on in situ measurements for calibration and validation. Improved stratospheric water vapor measurements remain much desired.

An airborne spectrometer can be deployed on an aircraft or a balloon. In fact, it is among the various techniques that have been applied for stratospheric

Corresponding author address: Maziar Bani Shahabadi, Department of Atmospheric and Oceanic Science, McGill University, Room 945, Burnside Hall, 805 Sherbrooke Street West, Montreal QC H3A 0B9, Canada.
E-mail: maziar.banishahabadi@mail.mcgill.ca

DOI: 10.1175/JTECH-D-13-00191.1

H_2O measurement. For example, an airborne far-infrared (FIR) interferometer was used to measure the stratospheric H_2O (Harries 1973). Comparing the intensity radiated by pairs of adjacent H_2O and O_2 lines, H_2O mass mixing ratio can be estimated, although an isothermal stratosphere and constant H_2O mixing ratio above the observer need to be assumed in the estimation. An airborne FIR radiometer was also used to measure the H_2O injected into the stratosphere by thunderstorms under similar assumptions (Barrett et al. 1973). The assumptions made for the water vapor retrieval are known to be unrealistic. To accurately monitor stratospheric H_2O, it is necessary to retrieve the vertical distributions of temperature and moisture altogether. This can be realized using a high-resolution infrared spectrometer (hyperspectrometer), which is capable of separating the two signals spectrally. Current state-of-the-art instruments include the Far-Infrared Spectroscopy of the Troposphere (FIRST) (Mlynczak et al. 2003), the Radiation Explorer in the Far Infrared (REFIR) (Palchetti et al. 2005), the Scanning High-resolution Interferometer Sounder (S-HIS) (Revercomb et al. 1998), and the Tropospheric Airborne Fourier Transform Spectrometer (TAFTS) (Canas et al. 1997). Among these hyperspectrometers, FIR coverage have been devised for TAFTS, REFIR, and FIRST [see Harries et al. (2008) for a review].

The H_2O concentration is much lower in the stratosphere than in the troposphere, which makes it challenging to retrieve stratospheric H_2O either from space or from on the ground. However, if an instrument is flown right below the stratosphere (at the tropopause), then by measuring the downward emission spectra of the stratosphere, the tropospheric obscuration is removed. In addition, in comparing to the occultation and limb sounding satellite measurements, an airborne measurement is of much smaller sampling volume and thus is advantageous of capturing small-scale variability. If such an instrument can operate in both uplooking and downlooking modes, then it can sound both the stratosphere and troposphere concurrently.

The goal of this paper is to examine the feasibility of retrieving the stratospheric H_2O profile, using a hypothetical uplooking spectrometer flying at the tropopause level. In section 2, the spectral signature of stratospheric H_2O in the tropopause downwelling longwave radiation is described. The simulation and retrieval methodology is described in section 3. In section 4, sounding of stratospheric temperature and H_2O profiles with different instrument specifications are compared. Also examined is how well a hypothetical sensor can detect stratospheric moistening episodes. The limitations are discussed in the concluding section.

2. Spectral signature of stratospheric H_2O

We first investigate the spectral signature of stratospheric H_2O in comparison to those of other atmospheric state variables, which illustrates the information in spectral measurements. To generate the spectral signals corresponding to realistic H_2O variability, we compare the spectrum simulated from the H_2O data of Anderson et al. (2012) that capture elevated stratospheric H_2O concentration caused by convective injection in summertime on the North America continent to the spectrum simulated from the standard midlatitude summer (MLS) profile (McClatchey et al. 1972). The MLS and Anderson profiles are shown in Fig. 1. The column H_2O loading (integrated from 100 to 1 hPa) of the Anderson and MLS profiles are 0.0046 and 0.0041 $kg\,m^{-2}$, respectively.

Downwelling radiance at 100 hPa is obtained by running the line-by-line radiative transfer model (LBLRTM, version 12.1) from Atmospheric and Environmental Research (AER) (Clough et al. 1992, 2005). The vertical resolution of the atmospheric profile input to LBLRTM is 2 hPa from 100 to 80 hPa, 5 hPa from 80 to 10 hPa, and 1 hPa from 10 to 1 hPa. High vertical resolution at 100–80 hPa is used to capture the highly variable water vapor concentrations around these levels. For molecular absorption, the Voigt profile is considered and all the H_2O continua are considered. No aerosol or solar input at the top of the atmosphere (TOA) is considered. The model calculates the emission spectrum between 200 and 2200 cm^{-1}, ignoring the scattering processes. Six molecular species are included in the calculation—namely, H_2O, CO_2, O_3, N_2O, CO, and CH_4, which are active gas species in the infrared region. The zenith angle is set to zero for a zenith-uplooking instrument.

Monochromatic radiance (output at a resolution of 0.001 cm^{-1}) is calculated with LBLRTM for the unperturbed (MLS) and the perturbed (Anderson) cases. The results are then convolved with a triangular spectral response function with the half-width at half maximum (HWHM) equal to 0.01, 0.1, 1, and 10 cm^{-1}. The results are shown in Fig. 2. Since H_2O is the only difference between the MLS and Anderson profiles, the spectral difference occurs only at H_2O absorption bands. The lower-stratospheric moistening affects the signal intensity in the water vapor rotational band (200–560 cm^{-1}) and the vibrational–rotational band (1350–1850 cm^{-1}). The 395–405 cm^{-1} spectral interval from the water vapor rotational band and the 1555–1565 cm^{-1} spectral interval from the vibrational–rotational band are enlarged for different HWHMs. These figures show that lowering the instrument spectral resolution (higher HWHM) will lower the signal intensity in the line center. The signal strength in the rotational band (FIR) is an order of magnitude

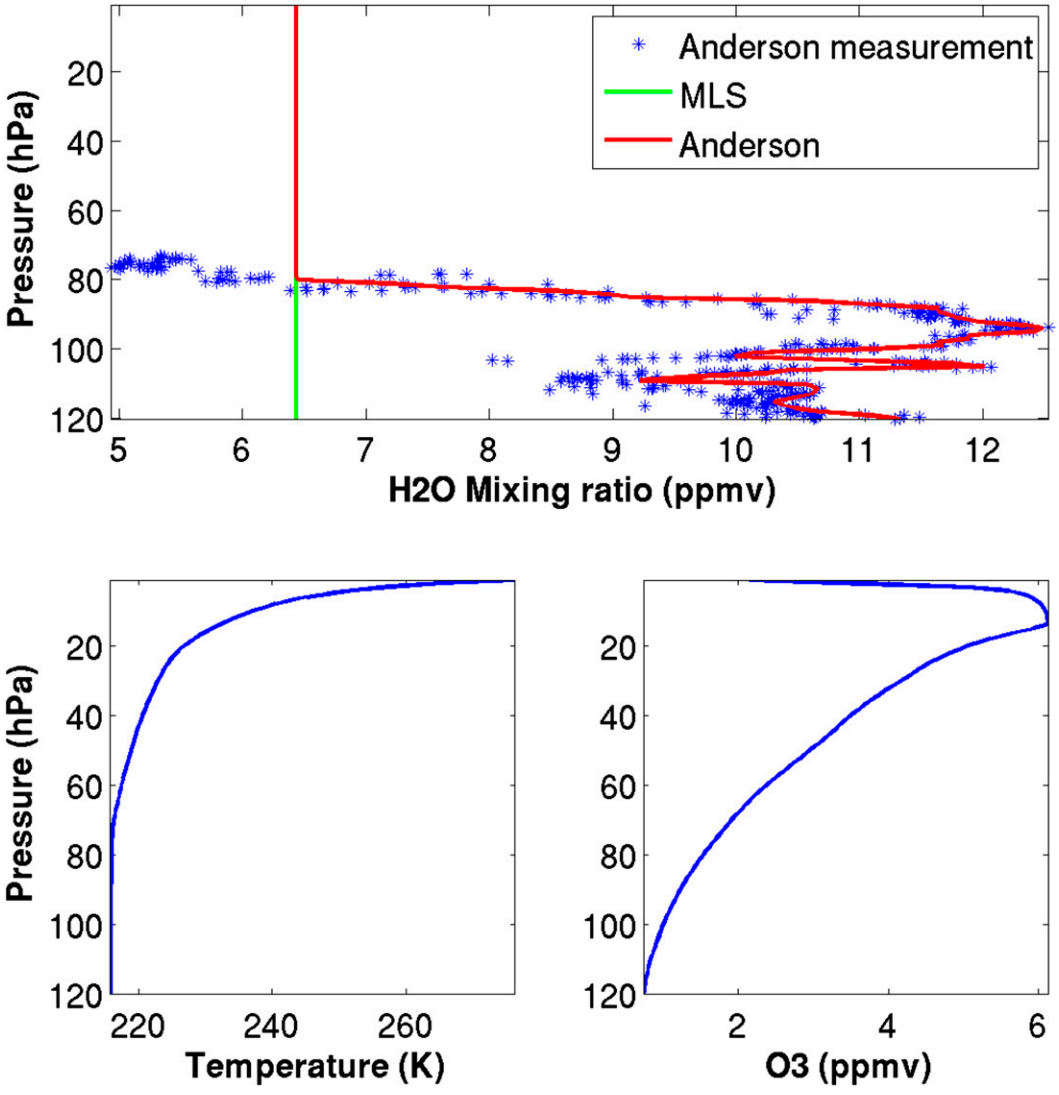

FIG. 1. H_2O profiles for MLS and Anderson profiles, plus temperature and ozone profiles.

stronger than the vibrational–rotational band, which is coincident with the upwelling signals of H_2O perturbation at the TOA (e.g., Harries et al. 2008). Given similar detector noise performance in the two bands, the rotational band is advantageous for measuring stratospheric H_2O. In section 4, we discuss how the spectral coverage and noise level impact stratospheric H_2O retrieval.

Other perturbation experiments are performed based on the MLS profile to examine the spectral signatures of temperature, CO_2, and O_3. The perturbations are prescribed as +1 K throughout the profile in temperature, +20 ppm in volume mixing ratio for CO_2, and +10% in O_3. The signal spectra from these experiments are compared with the H_2O signal obtained above (Anderson minus MLS). As Fig. 3 shows, temperature perturbation affects the CO_2 absorption band (600–800 cm^{-1}), the O_3 absorption band (1000–1200 cm^{-1}), and the H_2O rotational band (200–580 cm^{-1}). A change in CO_2 alters the radiance signal in the CO_2 absorption band, and O_3 modification mainly affects the O_3 absorption band. The comparisons here qualitatively show that the signal of H_2O is spectrally distinct from those of the other variables.

Furthermore, we test whether the different signals calculated above are linearly additive. Figure 3 shows that the sum of the signals due to individual perturbations can well reproduce the signal when all the perturbations are prescribed simultaneously. The difference between these two spectra is generally two orders of magnitude less than the overall change signal itself.

The spectral distinction of the different signals suggests that stratospheric H_2O and temperature may be retrieved simultaneously using an inverse method, such as the

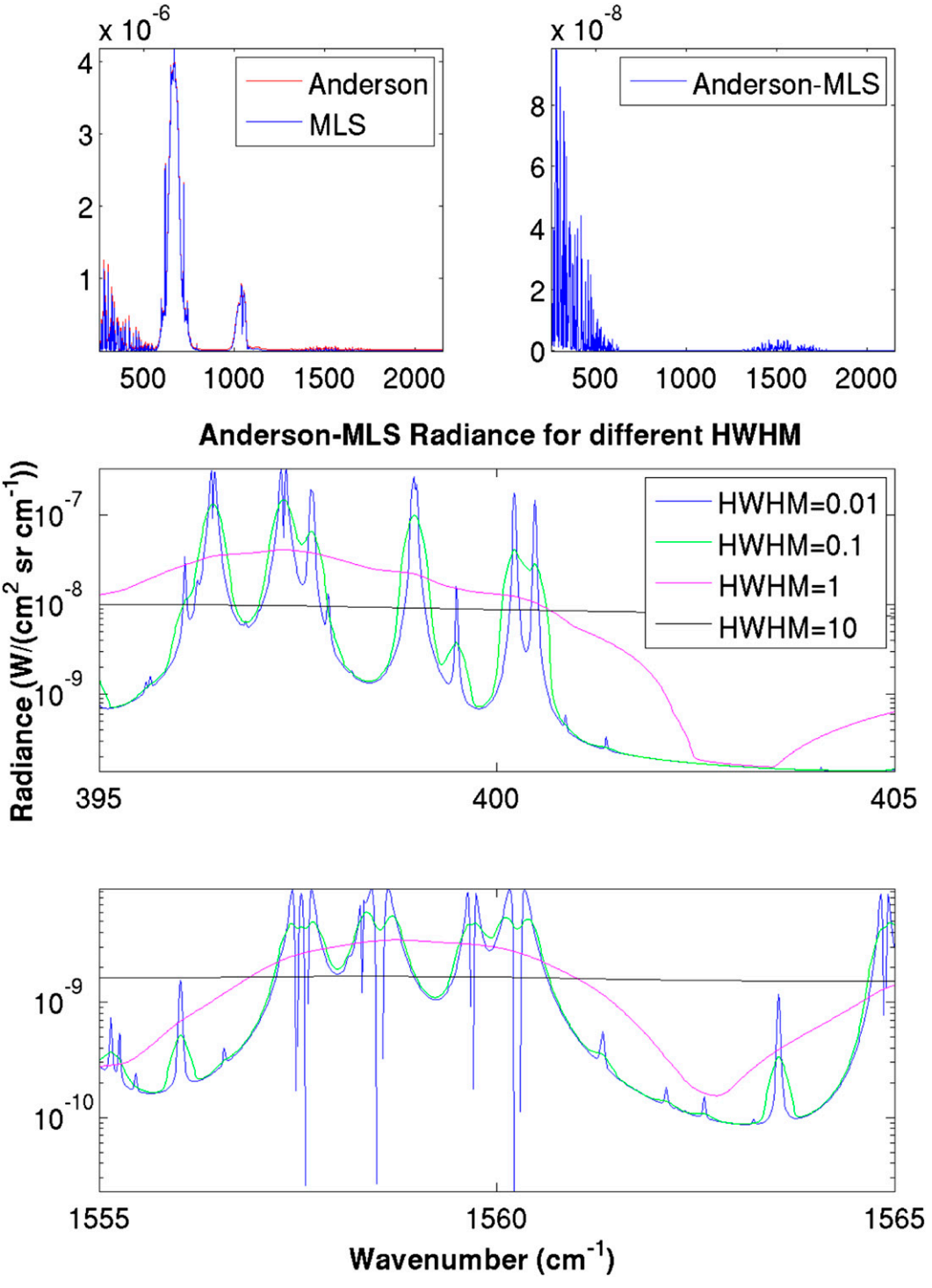

FIG. 2. Downwelling radiances at 100 hPa for MLS and convectively moistened (Anderson) profiles, and their difference at a spectral resolution of (top) HWHM = 1 cm^{-1}, and at varied HWHMs (cm^{-1}) for the spectral ranges of (middle) 395–405 and (bottom) 1555–1565 cm^{-1}.

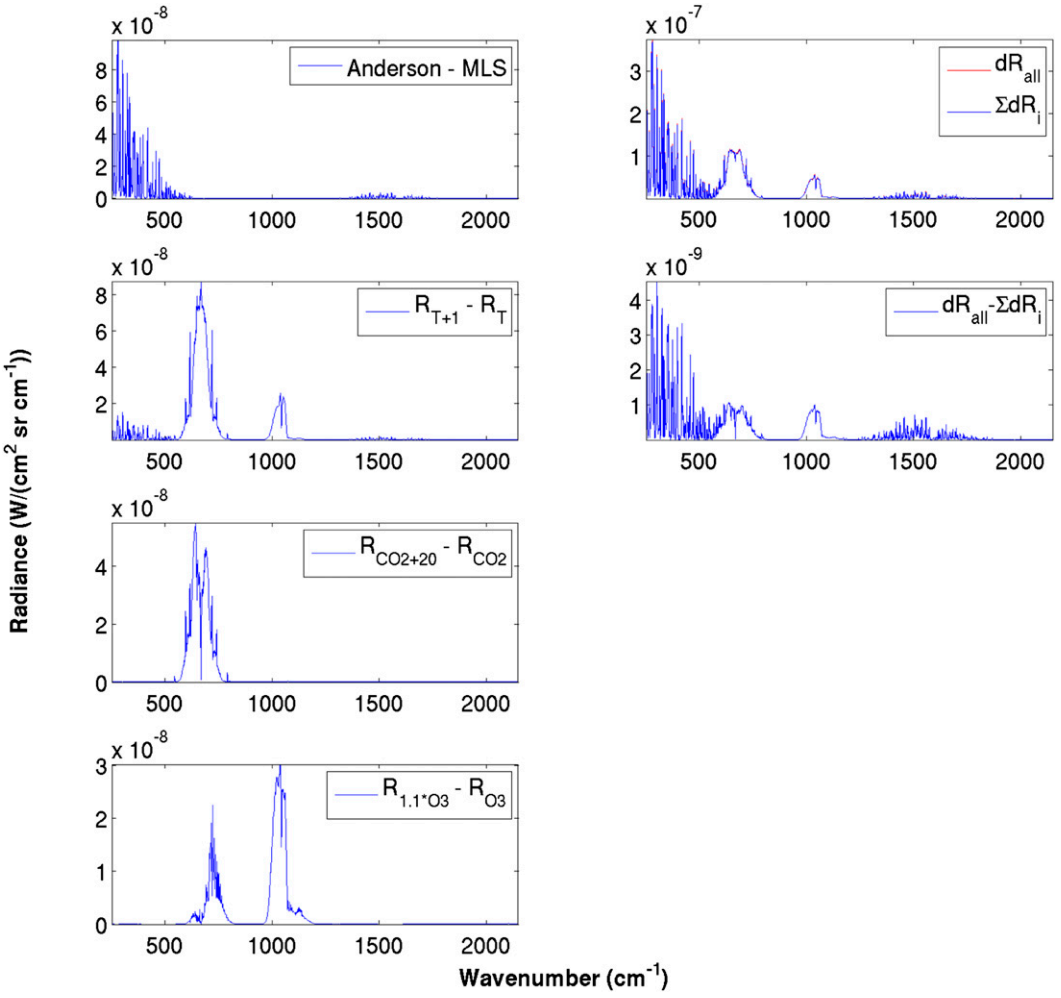

FIG. 3. (left) Comparison of spectral signature of the H_2O signal with perturbations of (second) temperature (+1 K), (third) CO_2 (+20 ppmv), and (fourth) O_3 (+10%). (top right) Comparison of change in downwelling radiance due to simultaneous change in all the variables (red line) and the sum of changes induced by each variable (blue line). (bottom right) Difference between red and blue lines in (top right).

optimal estimation method described by Rodgers (2000). The results also suggest that there is likely an advantage to using the FIR region, at high spectral resolution, for H_2O retrieval in particular.

3. Retrieval methodology

The retrieval methodology is based on the optimal estimation technique (Rodgers 2000). The linearized forward model can be described as

$$\mathbf{y} = \mathbf{y}_0 + \mathbf{K}_0(\mathbf{x} - \mathbf{x}_0) + \boldsymbol{\varepsilon} + \text{higher order terms}, \quad (1)$$

where $\mathbf{x}$ is the state vector to retrieve and $\mathbf{x}_0$ is the a priori (first guess) that is initially set to the mean of the climatology (training dataset). The elements of the state vector include temperature and the natural logarithm of water vapor mixing ratio at fixed vertical levels. Term $\mathbf{y}$ is the measurement (downwelling radiance measured at 100 hPa), and $\mathbf{y}_0$ is the radiance corresponding to state vector $\mathbf{x}_0$. The quantity $\mathbf{K}_0$ is the linearization of the forward model (Jacobian) computed at $\mathbf{x}_0$, and $\boldsymbol{\varepsilon}$ is the measurement error vector. The forward model used for radiance and Jacobian calculation is the LBLRTM version 12.1.

The iteration method is the Gauss–Newton method, which is a least squares method that minimizes the sum of the squares of residuals in the solution. The iteration formula is

$$\hat{\mathbf{x}}_{i+1} = \mathbf{x}_0 + (\mathbf{K}_i^{\mathrm{T}}\mathbf{S}_e^{-1}\mathbf{K}_i + \mathbf{S}_a^{-1})^{-1}\mathbf{K}_i^{\mathrm{T}}\mathbf{S}_e^{-1}[\mathbf{y} - F(\hat{\mathbf{x}}_i) + \mathbf{K}_i(\hat{\mathbf{x}}_i - \mathbf{x}_0)], \quad (2)$$

which computes a new estimate for the state vector ($\hat{\mathbf{x}}_{i+1}$) at each iteration. Term $\mathbf{K}_i$ is the Jacobian at the current state vector estimate, $\mathbf{S}_a$ is the a priori covariance of the

state vector, and $\mathbf{S}_e$ is the covariance of the measurement error. Term $F(\mathbf{x})$ is the forward model result, which is radiance. Terms $\mathbf{K}^{\mathrm{T}}$ and $\mathbf{K}^{-1}$ are for matrix transpose and inverse operations applied to matrix $\mathbf{K}$, respectively. The iteration proceeds until the convergence criteria are met or the number of iteration reaches 10. The convergence criteria are defined as

$$\hat{\mathbf{S}}^{-1} = \mathbf{K}_i^{\mathrm{T}}\mathbf{S}_e^{-1}\mathbf{K}_i + \mathbf{S}_a^{-1} \tag{3}$$

$$(\hat{\mathbf{x}}_{i+1} - \hat{\mathbf{x}}_i)^{\mathrm{T}}\hat{\mathbf{S}}^{-1}(\hat{\mathbf{x}}_{i+1} - \hat{\mathbf{x}}_i) < \mathrm{conv\_crit}, \tag{4}$$

where conv_crit is the convergence critical value. It is calculated by setting $(\hat{\mathbf{x}}_{i+1} - \hat{\mathbf{x}}_i)$ to the desired accuracy of 0.5 K for temperature and 0.05 ppmv for H_2O.

The atmospheric temperature and water vapor at 12 fixed pressure levels (10 hPa—spaced between 100 and 10 hPa, and then at 5 hPa and at 1 hPa) are considered for the retrieval here. In Eq. (2), the state vector has 24 elements with elements 1–12 corresponding to temperature and elements 13–24 corresponding to the logarithm of the water vapor mixing ratio. Stratospheric temperature and H_2O profiles obtained from the ACE-FTS instrument (Bernath et al. 2005) are used for testing the retrieval here. Only the North American profiles are selected. These profiles are selected in the region of 30°N < latitude < 60°N and 70°W < longitude < 130°W, between years 2004 and 2009. The temperature and H_2O profiles are interpolated to the 12 pressure levels. Overall, 286 temperature and H_2O profiles are retained after removing unrealistic profiles (those with high fluctuations in temperature/H_2O profiles, or decreasing temperature with altitude above the tropopause level). Out of the 286 profiles, 246 are randomly chosen and used to build the training dataset. The remaining unused 40 original ACE-FTS profiles are used as test cases and are referred to as the measurement dataset.

ACE-FTS is a solar occultation instrument, which measures infrared radiation at high spectral resolution (0.02 cm^{-1}) and spectral bandwidth from 750 to 4400 cm^{-1}. The satellite instrument samples atmospheric volumes that extend a few kilometers vertically and hundreds of kilometers horizontally (Bernath et al. 2005); thus, it does not capture smaller-scale atmospheric variability. To overcome this limitation of the dataset, we amend the dataset with artificially moistened profiles. To do so, each H_2O profile is perturbed by adding $x \times$ STD (H_2O) to a randomly selected 20-hPa-thick segment of the profile, where x is a random value drawn from the standard uniform distribution on the interval (0, 5) and STD (H_2O) is the H_2O standard deviation of the prior in that 20-hPa-thick segment. The perturbed H_2O profiles are then added to the original training dataset. The mean of all the training dataset is used as the a priori (first guess) in the retrieval tests. An a priori covariance matrix $\mathbf{S}_a$ is built using the enlarged training dataset (492 profiles). Figure 4 shows the correlation matrix of the training dataset. Figure 5 shows a subset of the measurement dataset chosen from the 45°–50°N latitudinal band as an example. The right panel shows the H_2O profiles that are artificially moistened. Note that the moistening prescribed here is very modest compared to the magnitude measured by Anderson et al. (2012).

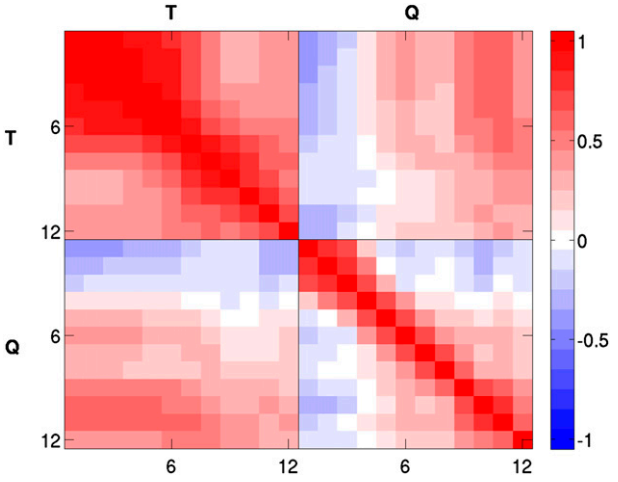

FIG. 4. Prior correlation matrix. The T–T and Q–Q portions show the corresponding temperature and log(H_2O) correlations, respectively; the T–Q portions shows the temperature and H_2O correlation. The tick labels on the axes correspond to the 12 vertical pressure levels used.

The sensor noise covariance $\mathbf{S}_e$ is assumed to be a diagonal matrix (uncorrelated noise). We start the analysis using a uniform noise magnitude equal to 0.25×10^{-7} W cm^{-2} sr^{-1} cm, which represents a very low noise detector. The magnitude of the noise will be varied to show the dependence of retrievals on the noise level. For every noise level, the random noise vector is generated and added to the synthetic radiance signal computed from the truth profile to mimic the sensor noise.

To account for the effect of spectral resolution on the retrieval outcome, all of the line-by-line calculations of radiance and Jacobian are performed with a monochromatic resolution of 0.001 cm^{-1}. Then they are convolved with the triangular scan function to spectral resolutions with the desired HWHM. The convolved radiance and Jacobian are used as input in the retrieval algorithm. Two spectral intervals are studied: 650–2200 and 200–2200 cm^{-1}. The first one represents the midinfrared (MIR), while the second one covers the full thermal infrared spectrum, including the FIR (below 650 cm^{-1}). The merit of each spectral interval for the retrieval of temperature and H_2O is examined and compared.

The quality of the retrieval is determined by a basic error statistic, the root-mean-square (RMS) of the errors.

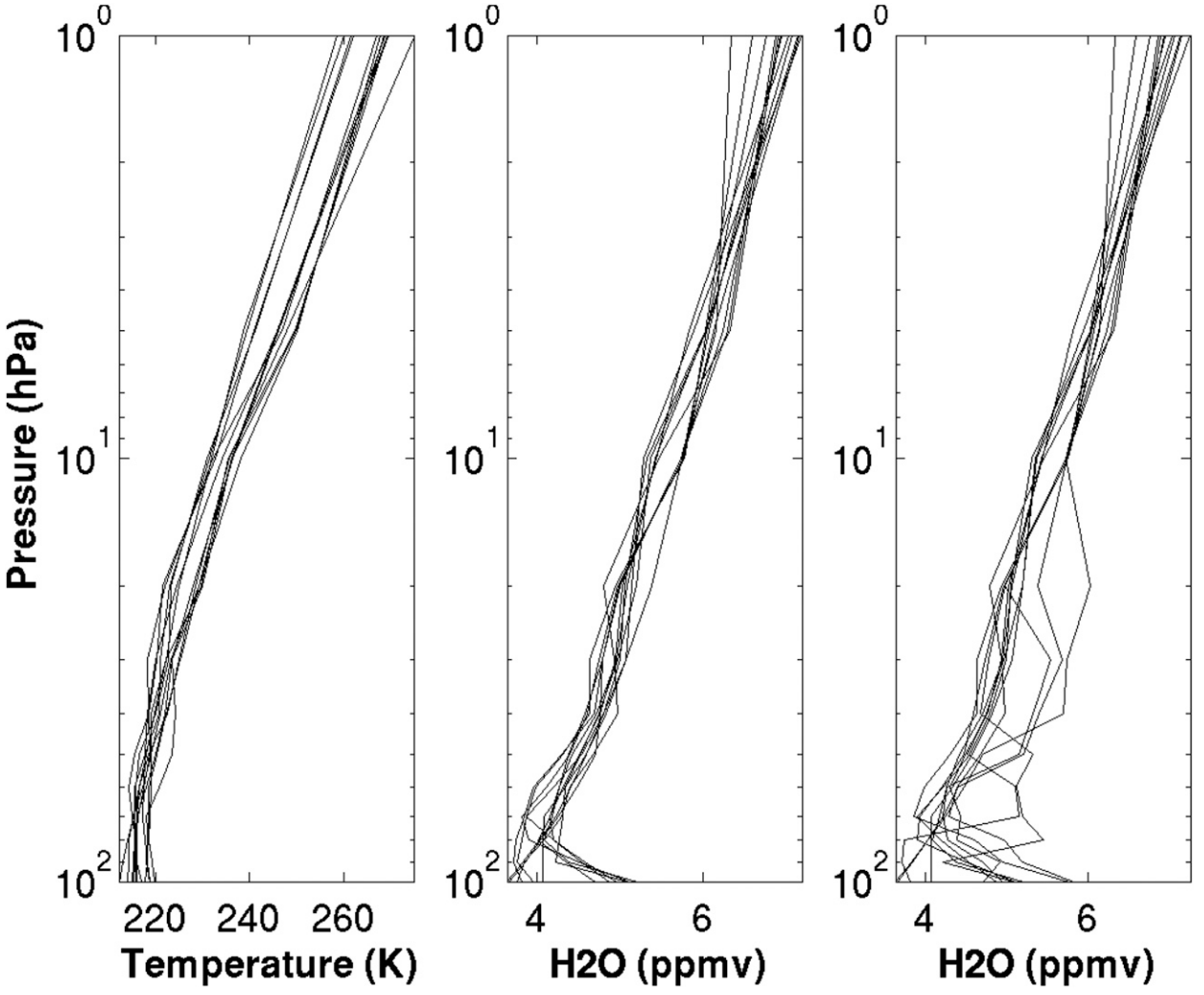

FIG. 5. Subset of (left) temperature and (middle) H_2O profiles for the 45°–50°N latitudinal band. (right) Artificially moistened H_2O profiles.

The retrieval accuracy is indicated by the RMS of the differences between the retrieved and truth quantities at each level for all of the test profiles; such an RMS profile, in comparison to the standard deviation (STD) of the training dataset (i.e., the a priori), also shows how the retrieval reduces the uncertainty in the atmospheric state. The retrieval precision is indicated by the STD of an ensemble of repeated retrievals of the same profile, where the simulated spectrum has been perturbed at a given noise level (the ''measurement error''; Rodgers 2000).

4. Sounding of stratospheric temperature/H_2O

a. *Ideal and realistic instruments*

The goal is to retrieve each truth profile by using the noise-added synthetic radiance spectrum computed from them. In other words, assuming that the synthetic radiance signal is sensed by the sensor, we examine how precisely the iteration technique can reproduce the truth profile. First, we restrict our retrieval test to the 40 unmoistened original ACE-FTS profiles.

To examine the potential of retrieving stratospheric H_2O and temperature simultaneously, we first analyze an ''ideal'' instrument, which has full IR coverage (200–2200 cm^{-1}), a high spectral resolution (0.1 cm^{-1}), and a very low noise level (0.25×10^{-7} W cm^{-2} sr^{-1} cm). The noise level mimics the desired performance of the Climate Absolute Radiance and Refractivity Observatory (CLARREO) instrument (Wielicki et al. 2013), similar to what is used by Merrelli and Turner (2012).

Figure 6 shows the spectral Jacobian for H_2O ($\mathbf{K}_q$) and temperature ($\mathbf{K}_T$). For information content assessment,

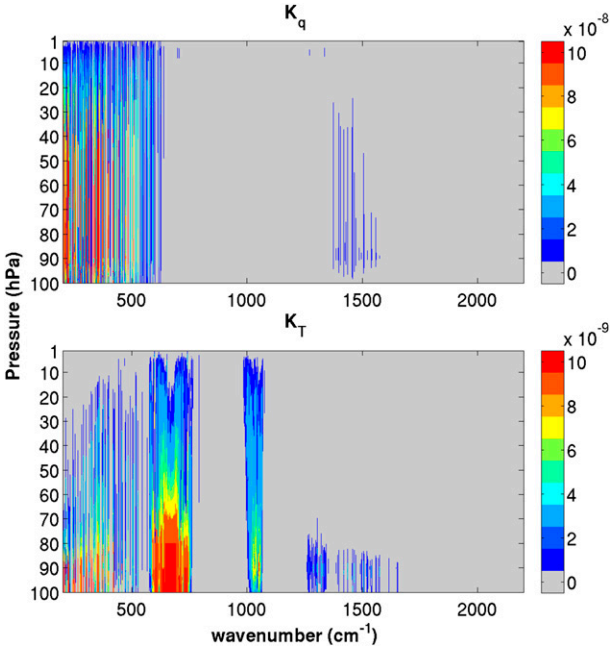

FIG. 6. Spectral Jacobian of (top) H_2O [$W\,cm^{-2}\,sr^{-1}\,cm\,\log(H_2O)^{-1}$] and (bottom) temperature ($W\,cm^{-2}\,sr^{-1}\,cm\,K^{-1}$).

the degrees of freedom for signal (DFS) is used, similar to the studies of the TOA spectra (e.g., Worden et al. 2004; Merrelli and Turner 2012). DFS is defined as the trace of averaging kernel matrix **A**, which, following Rodgers (2000), is formulated as

$$\mathbf{A} = (\mathbf{K}_i^{\mathrm{T}}\mathbf{S}_e^{-1}\mathbf{K}_i + \mathbf{S}_a^{-1})^{-1}\mathbf{K}_i^{\mathrm{T}}\mathbf{S}_e^{-1}\mathbf{K}_i. \quad (5)$$

Figure 7 shows the averaging kernel for temperature and H_2O. The rows 2, 5, 7, and 10 (out of 12), corresponding to different pressure levels, of the averaging kernels are shown. The total DFS is 1.8 and 4.4 for H_2O and temperature, respectively. The cumulative DFS (CDFS) normalized by the total DFS (Fig. 7c) shows that 100–40 and 100–10 hPa vertical segments contain 80% of the information for H_2O and temperature, respectively. The rows of the **A** matrix in Eq. (5) are the smoothing kernel that acts at each level in the retrieved state estimate, which indicates the vertical resolution in the retrieval results. The relatively low DFS and the broad shapes of **A** of the H_2O results from the relatively smaller magnitude of the H_2O Jacobian smoothing term ($\mathbf{K}_i^{\mathrm{T}}\mathbf{S}_e^{-1}\mathbf{K}_i$) compared to the inverse of the apriori covariance $\mathbf{S}_a^{-1}$.

Numerous tests are performed to examine the effects of changing the spectral resolution, spectral coverage, and noise level on the quality of the retrievals, and the results were compared to the retrieval by the above-mentioned ideal instrument. For example, in order to investigate the impact of the instrument noise, we adopt another noise level of $0.75 \times 10^{-7}\,W\,cm^{-2}\,sr^{-1}\,cm$ which, together with the lower noise level, encompasses the noise magnitude of the CLARREO instrument throughout the spectrum, to compare to the ideal case. These tests facilitate recommending a realistic sensor configuration that gives the desired retrieval results. Table 1 outlines a subset of the experiment cases that are investigated; Fig. 8 shows the corresponding results. Case 1 represents the ideal sensor setting. It has the highest DFS for temperature and H_2O (Table 1) and the lowest RMS error (red line in Fig. 8) among cases 1–5. Case 2 examines the impact of removal of FIR from case 1. The RMS error in the H_2O retrieval increases drastically and H_2O DFS drops to 0.6. The results here show that the FIR (below $650\,cm^{-1}$) is critical for the H_2O retrieval. This corroborates with the results from analysis of the spectral signature of stratospheric H_2O (section 2). Case 3 examines the impact of the increase in noise level of case 1. Case 4 verifies the effect of lower spectral resolution on the quality of the retrievals. Case 4 has a similar performance to case 3 for H_2O retrieval, but the temperature retrieval quality degrades compared to case 3, as shown by the temperature DFS value. Case 5 examines the impact of the combined effect of lower spectral resolution and higher noise level. The H_2O RMS error increases compared to cases 2–4, and H_2O DFS drops below one. Comparing case 5 to case 3, the finer spectral resolution appears to generate better temperature retrievals, especially in the upper stratosphere. Among all the cases with a noise level of $0.75 \times 10^{-7}\,W\,cm^{-2}\,sr^{-1}\,cm$, case 3 has an agreeable performance for both H_2O and temperature retrievals. Given these results, for further examination below, we focus on an instrument specified as case 3 and designate it as the "realistic sensor."

Besides the baseline measurement strategy (zenith uplooking at 100 hPa), a few additional instrument deployment strategies are examined. These include taking measurements at different zenith angles, taking measurements at multiple vertical levels, and taking multiple measurements under each atmospheric condition and conducting multiple retrievals and then averaging for the same condition. Our examination shows that changing the observation angle does not noticeably affect the RMS error statistics. Also, taking 10 measurements and averaging the retrievals under the same condition renders an equal performance compared to making one retrieval from the averaged spectral measurement, and neither shows significant improvement as judged by the RMS statistics. However, we find that adding measurement at an additional vertical level may considerably improve the retrieval performance; this is especially true for the H_2O

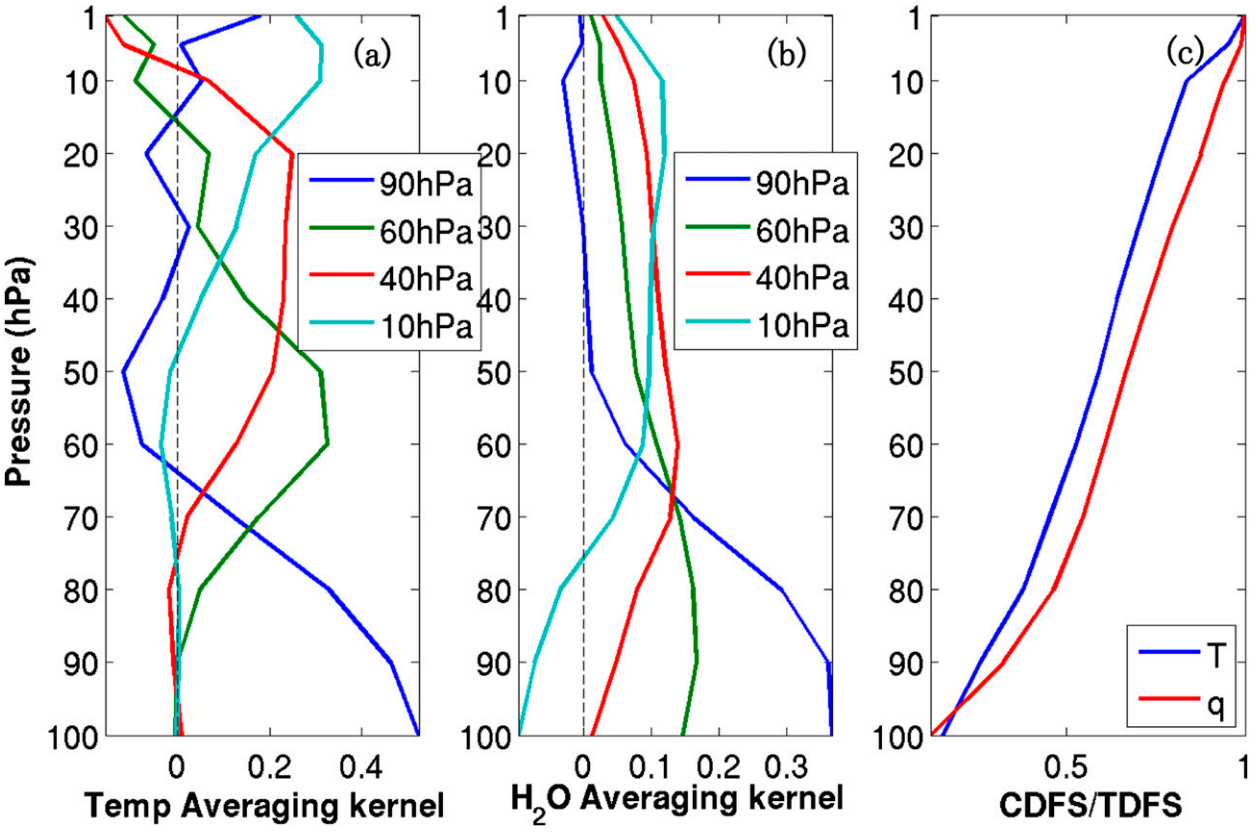

FIG. 7. Different rows of the averaging kernel matrix (corresponding to different pressure levels) for (a) temperature and (b) H_2O. (c) CDFS normalized with the total degree of freedom for signal (TDFS) for temperature and H_2O.

retrieval. Case 6 in Table 1 and Fig. 8 shows the information content increase for both temperature and H_2O when downwelling radiance spectra are obtained at both 100 and 90 hPa. This suggests that the retrieval can be optimized by flying the instrument to multiple altitudes at the same location.

In summary, we find that an infrared hyperspectrometer with a 200–2200 cm^{-1} spectral coverage, a 0.1 cm^{-1} spectral resolution, and a 0.75×10^{-7} $W\,cm^{-2}\,sr^{-1}\,cm$ noise level can generally achieve a retrieval accuracy of 0.2 ppmv for H_2O and 2 K for temperature up to about 20 hPa, and a precision of 0.02 ppmv for H_2O and 0.2 K for temperature. Such an IR spectrometer can afford a valuable in situ instrument for sounding the lower to midstratosphere.

b. Forward model error

The retrieval above only considers temperature and water vapor in each level; other trace gas species are set to fixed values and are not retrieved. If the trace gas profile

TABLE 1. Different test scenarios in Fig. 8.

RMS	Spectral resolution (cm^{-1})	Spectral coverage (cm^{-1})	Noise level ($W\,cm^{-2}\,sr^{-1}\,cm$)	Observer levels (hPa)	DFS temperature	DFS H_2O
Case 1 (ideal sensor)	0.1	200–2200	0.25×10^{-7}	100	4.40	1.76
Case 2 (without FIR)	0.1	650–2200	0.25×10^{-7}	100	4.32	0.60
Case 3 (higher noise)	0.1	200–2200	0.75×10^{-7}	100	3.53	1.19
Case 4 (lower resolution)	1	200–2200	0.25×10^{-7}	100	3.11	1.02
Case 5 (higher noise and lower resolution)	1	200–2200	0.75×10^{-7}	100	2.36	0.87
Case 6 (multialtitude)	0.1	200–2200	0.75×10^{-7}	100 and 90	4.47	2.06

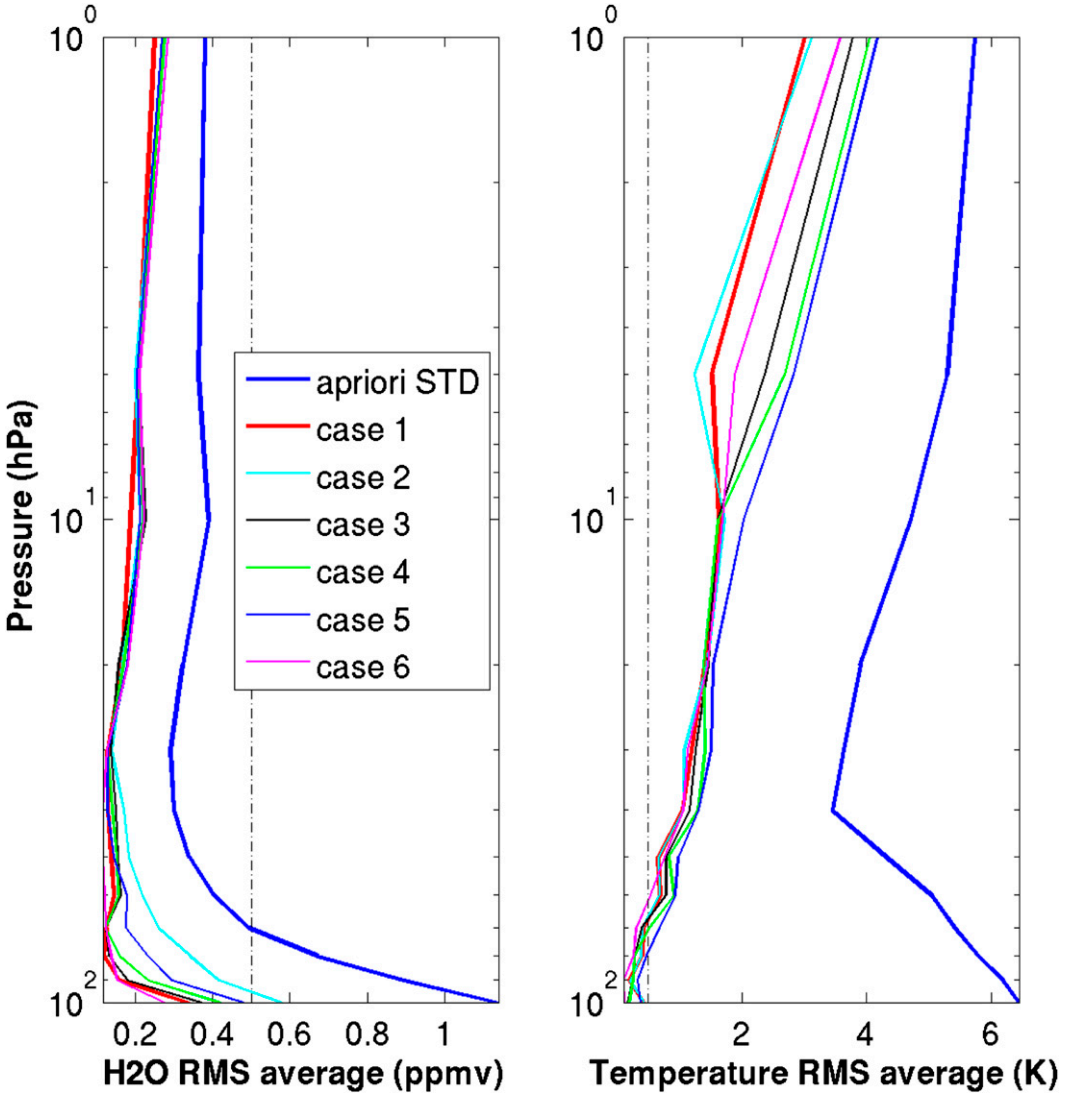

FIG. 8. Comparison of STD of a priori and retrieval RMS, for different sensor specifications. See Table 1 for a complete description of all cases.

is different from the assumed values, then the difference creates a forward model error. The effect of forward model error is examined here.

The forward model error analysis is performed separately for the primary gas species CH_4, N_2O, O_3, and CO_2. To apply a forward model error, the gas species concentration is perturbed with an additive error vector, randomly generated for each profile (the amplitude of the perturbation is 20 ppm for CO_2 and the STD of their variation is given by the ACE-FTS dataset for the other gases). The comparison for RMS error statistics of retrievals with and without forward model error implementation for different trace gas species is shown in Fig. 9. We find that although the errors in O_3 and CO_2 affect the quality of the temperature retrievals, the H_2O retrieval is largely unaffected.

Interestingly, we find that forward errors degrade the retrieval results more noticeably at the lower noise level (0.25×10^{-7} W cm^{-2} sr^{-1} cm), as the higher noise (0.75×10^{-7} W cm^{-2} sr^{-1} cm) acts to block out the impact of the forward errors prescribed here. This is confirmed by comparing the spectral signals due to each forward model error factor to the noise levels.

It is important to note that the impact of the forward error shown here represents the error one would get if naively ignoring the uncertainty in these gases, and that it can be minimized if these gases are simultaneously considered in the retrieval. Simultaneous multispecies

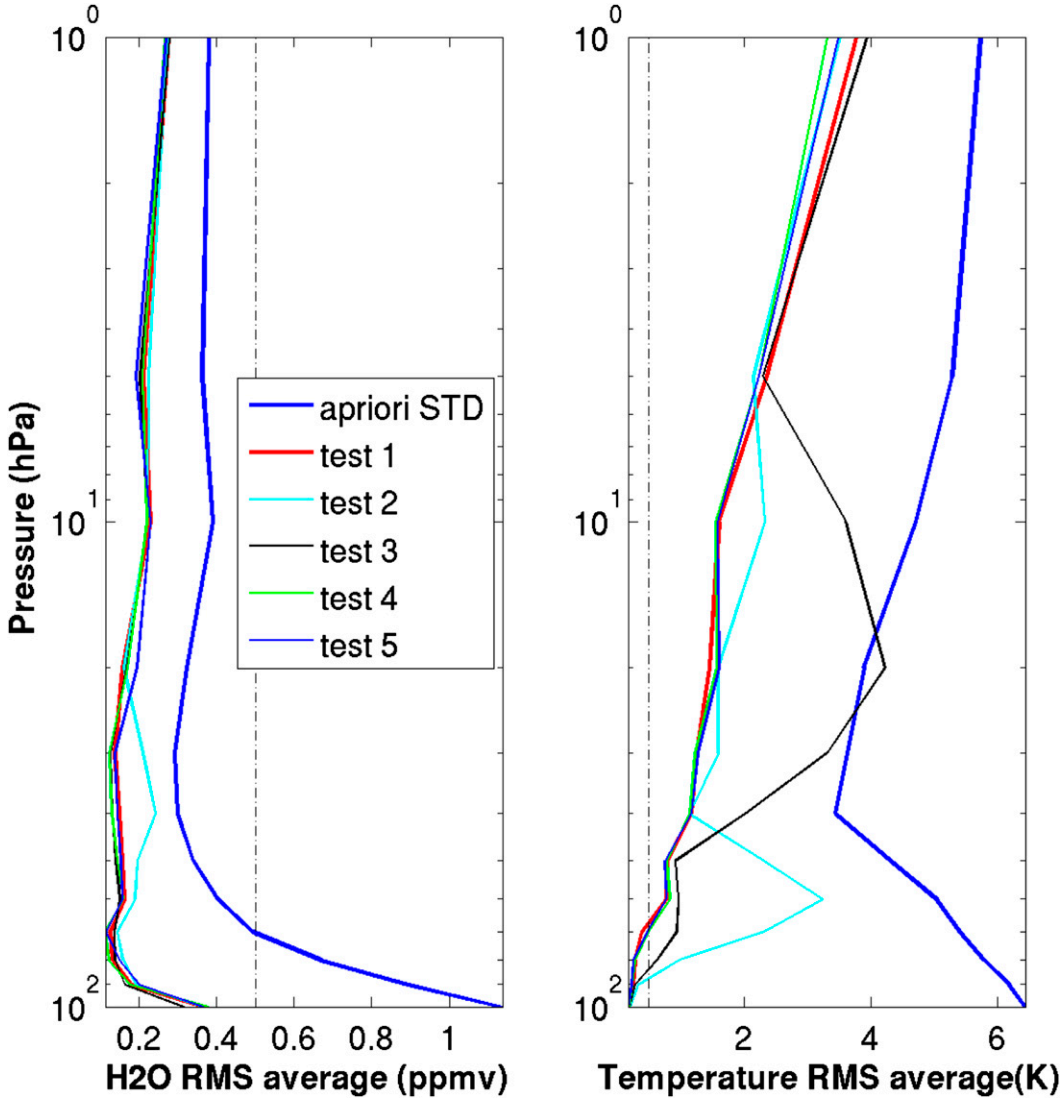

FIG. 9. Effect of forward model error on the retrieval RMS, for different gas species—test 1: realistic sensor with no forward model error, test 2: realistic sensor with CO_2 forward model error, test 3: realistic sensor with O_3 forward model error, test 4: realistic sensor with N_2O forward model error, and test 5: realistic sensor with CH_4 forward model error.

retrieval is beyond the scope of this paper, but we are interested in investigating this in future work.

c. *Detection of moistening*

Last, we test how well the stratospheric moistening episodes as identified by Anderson et al. (2012) can be detected using the recommended sensor. To conduct this test, we include in the retrieval the H_2O profiles that are artificially moistened from the 40 ACE-FTS test profiles, which extend the test to a total of 80 profiles.

The retrieval algorithm is performed using the *realistic* sensor configuration (case 3). The RMS error in the retrieval of truth profiles with and without moistened profiles is shown in Fig. 10. Although the RMS error in the moistened case is larger than the unmoistened case, it is considerably less compared to the uncertainty in the a priori guess. In general, a reduction in the uncertainty of more than 50% is achieved for the vertical distribution of water vapor; the retrieval accuracy is better than 0.4 ppmv for water vapor and 1 K for temperature up to 40 hPa. The RMS of the fractional error between the retrieved and truth H_2O loadings is 1.3% (unmoistened: 1.2%; moistened: 1.4%), which indicates that the measurement technique is very proficient at detecting moistening events. As an example, Fig. 11 demonstrates the retrieval of an arbitrarily selected profile, with and without moistening in the layer of 100–80 hPa. The results show that the retrieval

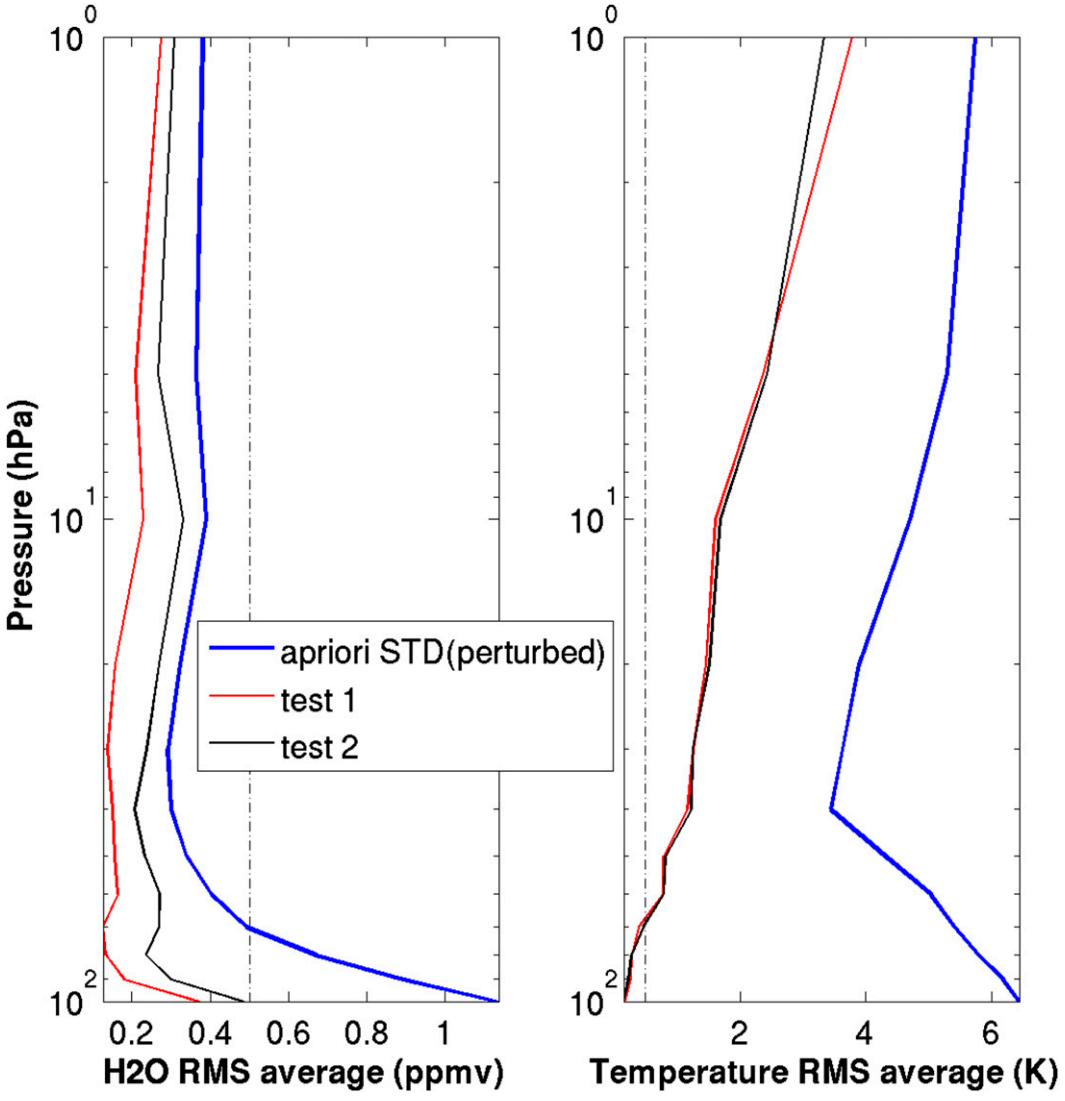

FIG. 10. Ability of realistic sensor to retrieve dry and moistened profiles—test 1: RMS of dry profiles retrievals and test 2: RMS of moistened profiles retrievals.

algorithm can well capture the H_2O concentration in both dry and moist cases.

5. Conclusions

Stratospheric H_2O is an important factor that affects climate change. Airborne infrared spectrometers are useful observational tools that may augment existing in situ and satellite observations. This study examines the feasibility of flying such a spectrometer at tropopause level to monitor stratospheric H_2O.

Observational data derived from the ACE-FTS satellite are used for testing this hypothetical instrument. Synthetic downwelling radiance is obtained by the LBLRTM radiation code. The Gauss–Newton iterative technique is used to obtain a solution from the retrieval algorithm. This study shows that a sensor with 200–2200 cm^{-1} spectral coverage, 0.1 cm^{-1} spectral resolution, and a noise level of 0.75×10^{-7} W cm^{-2} sr^{-1} cm is able to reach the accuracy of 0.4 ppmv and 1 K for simultaneous retrieving H_2O and temperature in the lower to midstratosphere. The retrievals become unreliable above 10 and 40 hPa for temperature and the H_2O, respectively. The results indicate that FIR, compared to MIR, is critical for profiling stratospheric H_2O, and a practical sensor needs to include this portion of the spectrum to successfully retrieve stratospheric H_2O. The forward model errors arising from uncertainties in CH_4, N_2O, O_3, and CO_2 do not significantly affect the H_2O retrieval, although there is a larger impact on

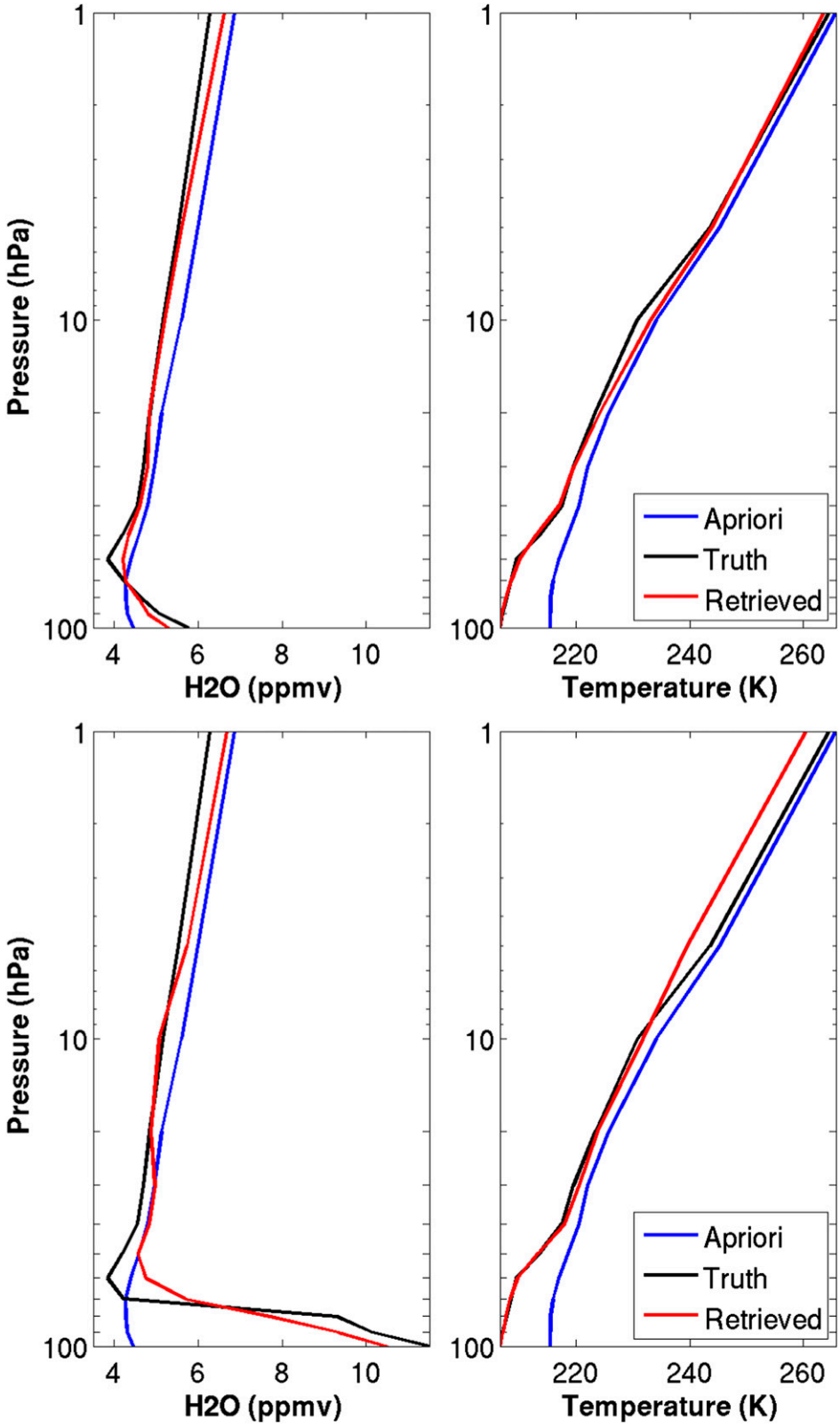

FIG. 11. Comparison of retrieval ability of realistic sensor for (top) dry and (bottom) moistened profiles for one case. The moistening is 2 times the original profile from 100 to 80 hPa.

the temperature results, especially for O_3 and CO_2 perturbations.

An airborne spectrometer has a fast response time and thus can capture the variability of water vapor on small temporal and spatial scales. This makes it an advantageous instrument for monitoring such lower-stratospheric moistening events, as documented by Anderson et al. (2012). The tests here show that the water vapor loading within the stratosphere can be detected to be within 1.3% uncertainty.

Acknowledgments. We thank David Turner and three anonymous reviewers, whose comments greatly helped improve this paper. This work is supported by the NSERC Discovery Program.

REFERENCES

Anderson, J. G., D. M. Wilmouth, J. B. Smith, and D. S. Sayres, 2012: UV dosage levels in summer: Increased risk of ozone loss from convectively injected water vapor. *Science,* **337,** 835–839, doi:10.1126/science.1222978.

Barrett, E. W., P. M. Kuhn, and A. Shlanta, 1973: Recent measurements of the injection of water vapor and ozone into the stratosphere by thunderstorms. *Proceedings of the Second Conference on the Climate Impact Assessment Program,* A. J. Broderick, Ed., National Technical Information Service, 34–46.

Bernath, P. F., and Coauthors, 2005: Atmospheric Chemistry Experiment (ACE): Mission overview. *Geophys. Res. Lett.,* **32,** L15S01, doi:10.1029/2005GL022386.

Canas, T. A., J. E. Murray, and J. E. Harries, 1997: Tropospheric Airborne Fourier Transform Spectrometer (TAFTS). *Satellite Remote Sensing of Clouds and the Atmosphere II,* J. D. Haigh, Ed., International Society for Optical Engineering (SPIE Proceedings, Vol. 3220), 91, doi:10.1117/12.301139.

Clough, S. A., M. J. Iacono, and J. Moncet, 1992: Line-by-line calculations of atmospheric fluxes and cooling rates: Application to water vapor. *J. Geophys. Res.,* **97,** 15 761–15 785, doi:10.1029/92JD01419.

——, M. W. Shephard, E. J. Mlawer, J. S. Delamere, M. J. Iacono, K. Cady-Pereira, S. Boukabara, and P. D. Brown, 2005: Atmospheric radiative transfer modeling: A summary of the AER codes. *J. Quant. Spectrosc. Radiat. Transfer,* **91,** 233–244, doi:10.1016/j.jqsrt.2004.05.058.

Forster, P. M. de F., and K. P. Shine, 1999: Stratospheric water vapour changes as a possible contributor to observed stratospheric cooling. *Geophys. Res. Lett.,* **26,** 3309–3312, doi:10.1029/1999GL010487.

Harries, J. E., 1973: Measurements of stratospheric water vapor using far-infrared techniques. *J. Atmos. Sci.,* **30,** 1691–1698, doi:10.1175/1520-0469(1973)030<1691:MOSWVU>2.0.CO;2.

——, and Coauthors, 2008: The far-infrared earth. *Rev. Geophys.,* **46,** RG4004, doi:10.1029/2007RG000233.

Kley, D., J. M. Russell III, and C. Phillips, Eds., 2000: SPARC assessment of upper tropospheric and stratospheric water vapour. WCRP-113, WMO/TD-1043, SPARC Rep. 2, 312 pp.

Livesey, N. J., and Coauthors, 2003: The UARS Microwave Limb Sounder version 5 data set: Theory, characterization, and validation. *J. Geophys. Res.,* **108,** 4378, doi:10.1029/2002JD002273.

McClatchey, R. A., R. W. Fenn, J. E. A. Selby, F. E. Volz, and J. S. Garing, 1972: Optical properties of the atmosphere. 3rd ed. Air Force Geophysical Laboratory Tech. Rep. AFCRL-72-0497, 80 pp.

Merrelli, A., and D. D. Turner, 2012: Comparing information content of upwelling far-infrared and midinfrared radiance spectra for clear atmosphere profiling. *J. Atmos. Oceanic Technol.,* **29,** 510–526, doi:10.1175/JTECH-D-11-00113.1.

Mlynczak, M. G., D. G. Johnson, and J. I. Applin, 2003: The Far-Infrared Spectroscopy of the Troposphere (FIRST) Project. NASA Earth Science Technology Conf. 2002, Pasadena, CA, NASA, 10 pp. [Available online at http://esto.nasa.gov/conferences/estc-2002/Papers/B4P2(Mlynczak).pdf.]

Oltmans, S. J., H. Vomel, D. J. Hofmann, K. H. Rosenlof, and D. Kley, 2000: The increase in stratospheric water vapor from balloonborne, frostpoint hygrometer measurements at Washington, D.C., and Boulder, Colorado. *Geophys. Res. Lett.,* **27,** 3453–3456, doi:10.1029/2000GL012133.

Palchetti, L., and Coauthors, 2005: Breadboard of the Fourier-transform spectrometer for the Radiation Explorer in the Far Infrared (REFIR) atmospheric mission. *Appl. Opt.,* **44,** 2870–2878, doi:10.1364/AO.44.002870.

Revercomb, H. E., and Coauthors, 1998: Recent results from two new aircraft-based Fourier-transform interferometers: The Scanning High-Resolution Interferometer Sounder and the NPOESS Atmospheric Sounder Testbed Interferometer. *Proc. Eighth Int. Workshop on Atmospheric Science from Space Using Fourier Transform Spectrometry,* Toulouse, France, CNES, 6 pp. [Available online at http://dreadnaught.ssec.wisc.edu/~shis/docsGEN/shisextabs.pdf.]

Rodgers, C. D., 2000: *Inverse Methods for Atmospheric Sounding: Theory and Practice*. Series on Atmospheric, Oceanic and Planetary Physics, Vol. 2, World Scientific Publishing, 240 pp.

Russell, J. M., III, and Coauthors, 1993: The Halogen Occulation Experiment. *J. Geophys. Res.,* **98,** 10 777–10 797, doi:10.1029/93JD00799.

Schwartz, M., W. G. Read, M. L. Santee, N. L. Livesay, L. Froidevaux, A. Lambert, and G. L. Manney, 2013: Convectively injected water vapor in the North American summer lowermost stratosphere. *Geophys. Res. Lett.,* **40,** 2316–2321, doi:10.1002/grl.50421.

Solomon, S., K. H. Rosenlof, R. W. Portmann, J. S. Daniel, S. M. Davis, T. J. Sanford, and G. K. Plattner, 2010: Contributions of stratospheric water vapor to decadal changes in the rate of global warming. *Science,* **327,** 1219–1223, doi:10.1126/science.1182488.

Thomason, L. W., S. P. Burton, N. Iyer, J. M. Zawodny, and J. Anderson, 2004: A revised water vapor product for the Stratospheric Aerosol and Gas Experiment (SAGE) II version 6.2 data set. *J. Geophys. Res.,* **109,** D06312, doi:10.1029/2003JD004465.

Weinstock, E. M., and Coauthors, 2009: Validation of the Harvard Lyman-α in situ water vapor instrument: Implications for the mechanisms that control stratospheric water vapor. *J. Geophys. Res.,* **114,** D23301, doi:10.1029/2009JD012427.

Wielicki, B. A., and Coauthors, 2013: Achieving climate change absolute accuracy in orbit. *Bull. Amer. Meteor. Soc.,* **94,** 1519–1539, doi:10.1175/BAMS-D-12-00149.1.

Worden, J., S. S. Kulawik, M. W. Shephard, S. A. Clough, H. Worden, K. Bowman, and A. Goldman, 2004: Predicted errors of tropospheric emission spectrometer nadir retrievals from spectral window selection. *J. Geophys. Res.,* **109,** D09308, doi:10.1029/2004JD004522.